Estimates of individual fracture compliances along boreholes from full-waveform sonic log data

Nicolás D. Barbosa[1,4], Andrew Greenwood[2], Eva Caspari[2], Nathan Dutler[3], and Klaus Holliger[4]

[1]Department of Earth Sciences, University of Geneva, Geneva, Switzerland
[2]Chair of Applied Geophysics, University of Leoben, Leoben, Austria
[3]Center for Hydrogeology and Geothermics, University of Neuchâtel, Neuchâtel, Switzerland
[4]Institute of Earth Sciences, University of Lausanne, Lausanne, Switzerland

Key Points:

- Fracture compliance is estimated from arrival time and amplitude differences of the critically refracted P-wave.
- The method is applied to FWS data acquired along a borehole penetrating moderately fractured crystalline rocks.
- The inferred fracture compliance profile highlights the most permeable fractures of the borehole.

Manuscript accepted for publication in J. Geophys. Res.: Solid Earth

Corresponding author: N. D. Barbosa, `nicolas.barbosa@unil.ch`

Abstract

An important seismic attenuation mechanism in fractured environments is related to energy conversion into reflected and transmitted waves at fracture interfaces. Using full-waveform sonic (FWS) log data, we show that it is possible to quantify transmission losses across a set of fractures from time delays and amplitude differences of the critically refracted P-wave as compared to intact sections along the borehole. In the presence of fractures, the transmission coefficient associated with a given fracture is obtained by combining information on transmission losses from multiple receivers and source positions into a linear system of equations for all fractures intersecting the borehole. Fracture compliance is computed from the inferred transmission coefficient based on a linear slip model. For validation, we use synthetic FWS log data obtained from numerical simulations of wave propagation in a water-filled borehole surrounded by low-permeability rocks with discrete fractures. The methodology is then applied to field data acquired along boreholes penetrating multiple fractures in a granodioritic host rock. We show that our estimations of mechanical compliance are consistent with previously reported values, which were estimated for individual fractures intersecting one of the boreholes with a related method valid only for isolated single fractures. Comparison between our estimates of fracture compliance and transmissivity profiles from previous hydraulic characterizations of the fractures suggests that the proposed method may also allow to locate the most permeable fractures along a borehole, which, in turn, opens the perspective of enhancing the design and effectiveness of subsequent hydraulic testing and fracturing experiments.

1 Introduction

Fractures are ubiquitous in upper crustal rocks. As potential fluid pathways, their presence can strongly influence many geological processes (e.g., earthquakes, volcanic activity, hydrothermal flow) as well as associated human activities (e.g., development of hydrocarbon and geothermal reservoirs, CO_2 and nuclear waste storage, construction of tunnels and dams) (e.g. Gudmundsson, 2011). For this reason, the use of remote-sensing-type geophysical techniques for fracture detection and characterization is of great interest. In particular, the well known influence of fractures on the travel times and amplitudes of seismic waves makes associated techniques valuable tools for fracture network imaging, characterization, and monitoring (e.g. National Research Council, 1996; Liu & Martinez, 2013). Furthermore, several authors point to the existence of an interdependence between the mechanical (e.g., compliance) and hydraulic (e.g., transmissivity) properties of fractures, which, in turn, has motivated the development of methods for predicting the hydraulic response of fractures from seismic signatures (Pyrak-Nolte & Morris, 2000; Bakku et al., 2013).

The seismic signature of fractured rocks is defined by the relation between the characteristic size and spacing of fractures and the prevailing seismic wavelengths. When the wavelength is much larger than the fractures, the characteristics of seismic wave propagation through the fractured medium are described by an effective stiffness tensor, which, in general, can be anisotropic (e.g. Gurevich, 2003; Hudson, 1980; Schoenberg & Douma, 1988) with complex-valued and frequency-dependent elements (e.g. Chapman, 2003; Rubino et al., 2013). In this context, methods based on amplitude and/or velocity variations with offset and/or azimuth are typically used to characterize the effective mechanical behavior of sets of fractures (e.g. Lubbe & Worthington, 2006; Fang et al., 2016; Barbosa, Köpke, et al., 2020). When the wavelength becomes comparable to the distance between fractures and their characteristic length, fractures are seismically characterized as discrete features (Schoenberg & Douma, 1988). The detection and analysis of these macro-fractures is particularly relevant as they tend to dominate the hydraulic behavior of the associated subsurface volume (Bakku et al., 2013). Theoretical and experimental works have shown that the scattering of seismic wavefields due to the presence of isolated fractures can significantly affect their amplitudes and velocities (e.g. Morris et al., 1964; Pyrak-Nolte et al., 1990b; Worthington & Hudson, 2000; Minato & Ghose, 2016), which, in turn, allows for mechanical characterization of the fractures.

In spite of the potential of seismic data to provide hydraulic information on fractures, field-scale studies providing evidence and insights on this relation are still scarse and, so far, most studies on the hydromechanical behavior of fractures using seismic methods have been performed on numerical samples (e.g., Pyrak-Nolte & Morris, 2000; Kang et al., 2016; Pyrak-Nolte & Nolte, 2016). Arguably, the main reason for this is that the hydromechanical interdependence, which is not known a priori, depends on complex geometrical aspects of the fractures (e.g., spatial correlation of the fracture aperture distribution) that can only be known with sufficient accuracy for synthetic samples. This problem can be potentially alleviated by studying fractures intersecting a borehole as they can be mechanically and hydraulically characterized under well-controlled conditions. The hydraulic characterization of fractures typically consists of estimating effective transmissivity, storativity, and/or diffusivity through either conventional transient tests, such as, for example, constant head, constant flow, slug, pulse, and recovery tests (e.g., Dutler et al., 2019; Brixel et al., 2020; Krietsch et al., 2020) or periodic pumping tests (e.g., Y. Cheng & Renner, 2018). On the other hand, various borehole geophysical methods are commonly employed for fracture mechanical and geometrical characterization including, for example, geophysical logging, vertical seismic profiling (VSP), and ground penetrating radar (GPR) surveys (e.g., National Research Council, 1996; Doetsch et al., 2020; Shakas et al., 2020). As an example, following a long-wavelength approach, Prioul et al. (2007) and Prioul and Jocker (2009) quantified the mechanical effects of natural and drilling-induced fractures along a borehole using conventional full-waveform sonic (FWS) data. Using P- and S-wave slownesses, the authors inferred a single effective compliance value characteristic of each fracture type. However, even under well-known and well-controlled experimental conditions, conventional interpretation methods often do not allow for estimating the compliances of individual fractures. Thus, a necessary first step to improve our understanding of the hydromechanical behavior of fractures is the development of new seismic methods, which, exploiting the advantages of common borehole setups, allow for estimating the compliances of individual fractures.

Following this idea, Bakku et al. (2013) presented a method to estimate fracture compliance, aperture, and length using the amplitude ratio of the pressure due to a fracture-related tube wave and the corresponding incident P-wave. They reported compliance estimations for a single fracture intersecting a borehole using amplitudes recorded during a VSP experiment. Also using VSP data, Hunziker et al. (2020) developed a Bayesian Markov chain Monte Carlo (MCMC) full-waveform inversion algorithm to simultaneously infer hydraulic (i.e., aperture) and mechanical (i.e., compliance) characteristics of individual fractures from tube wave signals. The authors considered a subsection containing 3 fractures of a VSP dataset acquired along a borehole at the Grimsel Test Site (GTS) in Switzerland and estimated fracture compliance and hydraulic aperture as well as the elastic moduli of the background rock. The results showed that, due to the close spacing, the hydraulic apertures of individual fractures could not be determined, which hindered a quantitative analysis of their hydromechanical responses. Barbosa et al. (2019) proposed a method to estimate the mechanical compliance of isolated fractures intersecting a borehole using P-wave velocity changes and transmission losses inferred from FWS log data. In the given context, transmission losses refer to the conversion of the incident wave into reflected and transmitted waves at a given fracture. Using the spectral ratio and phase difference techniques to estimate attenuation and velocity, respectively, in an interval between two receivers bounding a fracture, they reported compliance estimates for 5 isolated fractures intersecting a borehole at the GTS. Interestingly, the highest compliance values were associated with fractures for which strong tube waves were excited in the VSP experiment reported by Hunziker et al. (2020). This correlation was attributed to the expected scaling between hydraulic and mechanical properties of fractures, according to which hydraulically open fractures tend to be more compliant (Pyrak-Nolte & Nolte, 2016).

In this work, we propose a new method to estimate fracture compliance profiles along a borehole from FWS data. The method is a generalization of the one of Barbosa et al. (2019) for individual, well-separated fractures. Another important and potentially error-prone aspect of the method of Barbosa et al. (2019) is the need to correct attenuation estimates for mechanisms other than transmission losses, such as, for example, geometrical spreading, in order to isolate the effects of fractures. To alleviate this problem, we propose to infer P-wave transmission coefficients associated with the presence of fractures from the amplitude ratios and time delays obtained when comparing the critically refracted P-wave signal in fractured and intact sections along the borehole. The assumptions behind this method are that the amplitude decay due to geometrical spreading is similar in both cases, which implies that the corresponding corrections of the overall amplitude decay are no longer necessary and that the intact sections provide the necessary information on the embedding background medium of the fractured sections. Moreover, an independent estimate of the transmission coefficient of a set of fractures is obtained for each receiver. Then, by exploiting the corresponding redundancy of transmission coefficient information obtained from multiple receivers, we relax the single-fracture assumption of Barbosa et al. (2019) and estimate effective mechanical compliance for sets of fractures intersecting the borehole. The newly proposed methodology is validated using synthetic FWS log data representative of a section of an open borehole intersecting multiple fractures. We then proceed to apply the method to FWS datasets from two boreholes at the GTS, which penetrate a granodioritic rock mass intersected by multiple fractures. We also compare the estimated compliance profile with corresponding transmissivity estimates from hydraulic tests to explore the potential of the former with regard to identifying the most permeable sections along a borehole.

2 Methodology

For the following, we shall consider a FWS experiment, in which a monopole source creates a pressure perturbation in the center of a water-filled borehole. The associated wavefields consisting mainly of critically refracted P- and S-waves, and Stoneley waves, which are commonly referred to as tube waves (e.g. Toksoz et al., 1983; Haldorsen et al., 2006; Durán et al., 2018), are sampled by pressure sensors along the borehole. In this work, we consider the critically refracted P-wave in general and its amplitude and velocity characteristic in intact and fractured rocks in particular.

The amplitude spectrum of the critically refracted P-wave can be modelled as (Sun et al., 2000)

$$A(\omega, r) = F(\omega, r_s, r) G(\omega, r_s, r) \exp(-\frac{\omega}{2} Q_p^{-1} \Delta t_r), \tag{1}$$

with ω denoting the angular frequency; r_s and r are the depth coordinate of the source and the receiver, respectively; Q_p^{-1} and Δt_r are the effective attenuation (without geometrical spreading contribution) and P-wave travel time between the source and the receiver, respectively; G is the geometrical spreading function; and F is a function accounting for source and receiver spectra and corresponding coupling terms, which are associated with signal transmission losses at the borehole wall.

2.1 Compliance estimation from transmission losses

The mechanical compliance of fractures is estimated from the P-wave transmission coefficient T associated with them, which, in turn, can be expressed as (Barbosa et al., 2019)

$$T = e^{i(k_p^b - k_p^{eff})\Delta r}, \tag{2}$$

where k_p^b and k_p^{eff} denote the P-wavenumbers of the intact background rock and the fractured section, respectively, and Δr is the propagating distance. Following Barbosa et al. (2019), the functions G and F in Eq. 1 are expected to be similar for intact and fractured rock. In this scenario, we can approximate the transmission coefficient of the fractured section in Eq. 2 as

$$T = e^{-\ln[A^b/A^{eff}]+i\omega\delta t}, \tag{3}$$

with $A^b(\omega, r)$ and $A^{eff}(\omega, r)$ being the amplitude spectra of the critically refracted P-wave after propagating through intact and fractured rock, respectively, and δt the P-wave arrival time difference between propagation in intact and fractured rock. We compute δt at the nominal source frequency and use the sign convention for which $\delta t >0$ in the presence of compliant fractures. The ratio $\ln[A^b/A^{eff}]$ is a typical indicator of amplitude decay (e.g. C. H. Cheng et al., 1982; Molyneux & Schmitt, 2000; Milani et al., 2015). An advantage of using Eq. 3 instead of Eq. 2, as in Barbosa et al. (2019), to compute T is that we avoid the estimation of phase velocity and attenuation corrections due to, for example, geometrical spreading.

For a critically refracted P-wave that propagates across a set of aligned fractures having individual transmission coefficients t_i, the magnitude of the bulk transmission coefficient of the fracture set T given by Eq. 3 can be written as (Pyrak-Nolte et al., 1990a)

$$T = \prod_i^N t_i, \tag{4}$$

where N is the number of fractures located in the interval between the source and the receiver, which can be known in advance, for example, from core analyses and/or televiewer data. Note that for each source-receiver position, we obtain a single transmission coefficient T representative of the set of fractures located between the source and the receiver. In order to estimate the N individual transmission coefficients t_i, we solve a system of equations, in which the number of equations N_T is at most the number of source locations times the number of receivers

$$\left\{\begin{array}{ccccccccc} a_{1,1}\log(t_1) & + & a_{1,2}\log(t_2) & + & \cdots & + & a_{1,N}\log(t_N) & = & \log(T_1) \\ a_{2,1}\log(t_1) & + & a_{2,2}\log(t_2) & + & \cdots & + & a_{2,N}\log(t_N) & = & \log(T_2) \\ \vdots & & \vdots & & \ddots & & \vdots & & \vdots \\ a_{N_T,1}\log(t_1) & + & a_{N_T,2}\log(t_2) & + & \cdots & + & a_{N_T,N}\log(t_N) & = & \log(T_{N_T}) \end{array}\right. . \tag{5}$$

In Eq. 5, the matrix coefficients $a_{i,j}$ are equal to 1 if t_i contributes to T_j and 0 otherwise. Again, the contribution of the i-th fracture to the overall T_j can be determined from core analyses and televiewer data for given positions of the source and the receivers. Each row, or equation, in the linear system of Eq. 5 represents a source-receiver combination along the borehole for which a transmission coefficient can be computed. That is, a receiver's position, at which

1- there is at least one fracture between the source and the receiver;

2- the refracted P-wave arrives later in fractured than intact sections, as we deal with fractures that are more compliant than the embedding medium;

3- the closest fracture below and above the receiver is located at a distance larger than 3/2 and 1/2 of the P-wavelength, respectively (note that we assume that the source is always below the receivers) to reduce effects of other wave modes (please refer to Section 3.1 of the manuscript for more details on this condition);

4- there are no damage-related features (e.g., S3-type shear zone) between the source and the receiver except for fractures.

The number of rows in the system of Eqs. 5 is thus given by the number of source locations times the number of receivers meeting the above-mentioned conditions. Finally, by solving the linear system of Eqs. 5, we can thus estimate the individual t_i values for all the observed fractures.

Table 1. Physical properties of background rock, fractures, and fluid.

Physical property	Background	Fracture 1	Fracture 2	Fracture 3
Dry frame bulk modulus K_m [GPa]	33	0.056	0.056	0.056
Dry frame shear modulus μ_m [GPa]	29	0.033	0.033	0.033
Porosity ϕ [-]	0.004	0.1	0.5	0.75
Permeability κ [mD]	0.5	100	100	100
Solid grain bulk modulus K_s [GPa]	37	37	37	37
Solid grain density ρ_s [Kg/m^3]	2730	2730	2730	2730
Fluid bulk modulus K_f [GPa]	2.25	2.25	2.25	2.25
Fluid density ρ_f [Kg/m^3]	1000	1000	1000	1000
Fluid viscosity η [Pa s]	0.001	0.001	0.001	0.001
Aperture h [mm]	–	5	5	10

Lastly, we assume a linear slip model to represent the seismic effect of fractures, which are conceptualized as planes of weakness that produce a seismic displacement jump proportional to their mechanical compliance. In this scenario, the compliance of a fracture Z_{N_i} can be estimated from the transmission coefficient t_i as (Schoenberg, 1980)

$$Z_{N_i} = \frac{(1-t_i)}{it_i}\frac{2}{\omega I_b}, \tag{6}$$

where $I_b = \rho_b v_p^b$ is the impedance of the intact background rock. Note that Eq. 6 is strictly valid for normal P-wave incidence, in which case Z_{N_i} corresponds to the so-called normal compliance of the fracture.

Barbosa, Caspari, et al. (2020) compared the results of the method given by Eqs. 3 to 6 with those obtained using the methodology presented in Barbosa et al. (2019) to show that both methods provide similar results for the case of an isolated single fracture. In the following, we apply the newly proposed method to synthetic and observed FWS data acquired across multiple, closely spaced fractures.

3 Results

3.1 Synthetic data set

To validate the proposed methodology of fracture compliance estimation, we reproduce a FWS experiment under open borehole conditions by performing numerical simulations of seismic wave propagation based on Biot's (1962) dynamic equations for a rotationally symmetric medium (Sidler et al., 2013b, 2013a). In Fig. 1, we show examples of the numerically recorded pressure fields for an intact (Fig. 1a) and a fractured formation (Fig. 1b). We have considered a single source position at 0.5 m depth and, for illustration purposes, pressure recordings are sampled every 5 mm along the borehole. In general, however, pressure sensors in a FWS tool are spaced at ∼1 ft intervals. The nominal source frequency is $f = \omega/2\pi$=20 kHz. The chosen material properties representing a low-porosity crystalline background rock and the highly compliant, porous, and permeable fractures are given in Table 1. The solid grain and fluid properties are assumed to be the same for the fractures and the embedding background (Table 1). Fig. 1b clearly shows that, when a critically refracted P-wave travelling along the borehole hits a fracture, it creates tube waves and other reflected and transmitted wave modes, which, in turn, manifests itself in a more complex pressure field compared to the non-fractured medium (Fig. 1a).

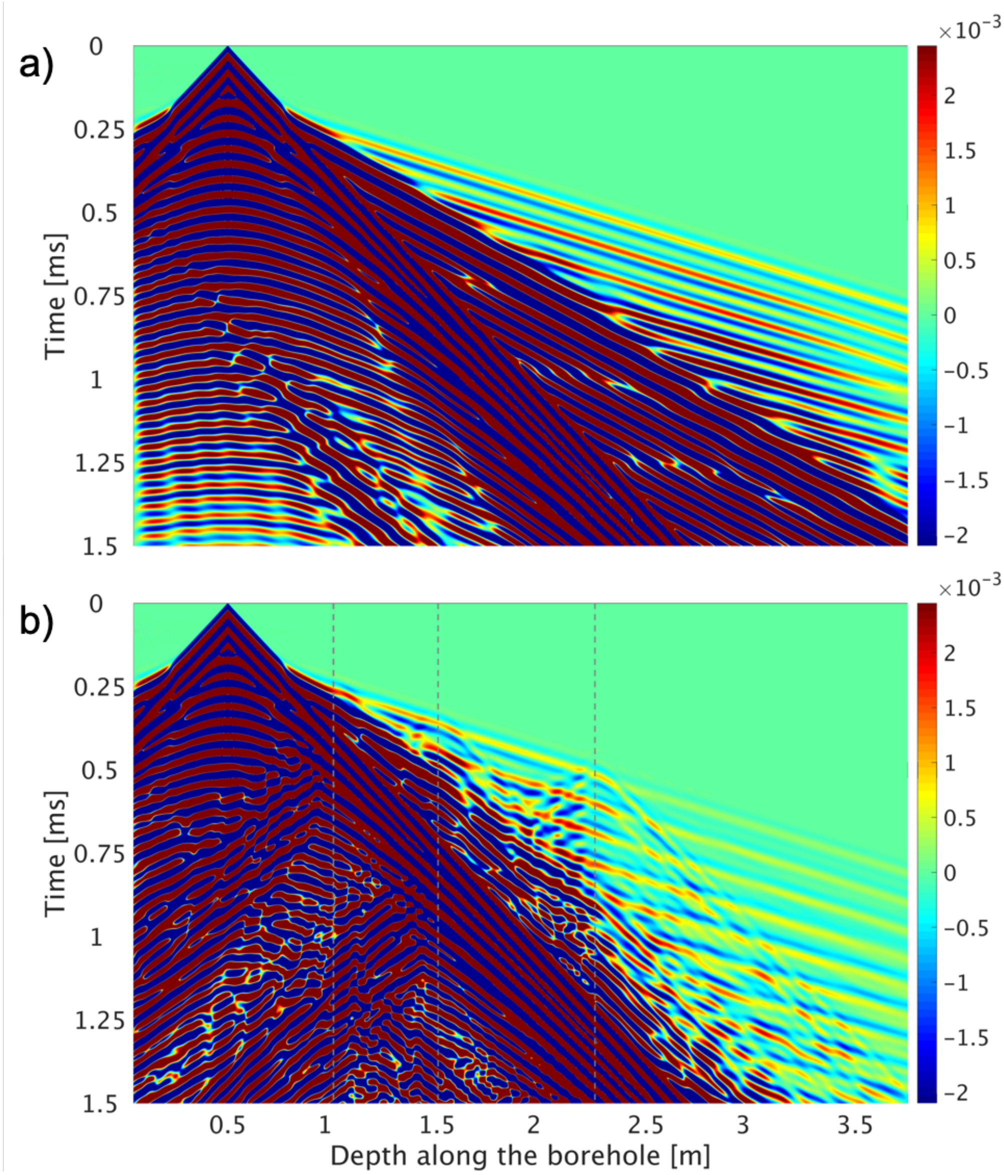

Figure 1. Numerical FWS-type simulation of fluid pressure recordings at the center of a numerical water-filled borehole as functions of time and depth. The source is located at 0.5 m depth and emits a compact pulse with a nominal center frequency of 20 kHz. The borehole is surrounded by (a) intact and (b) fractured crystalline rocks. Vertical dashed lines in (b) illustrate the location of the fractures. For illustration purposes, the traces are normalized with respect to the overall maximum pressure recorded in each experiment.

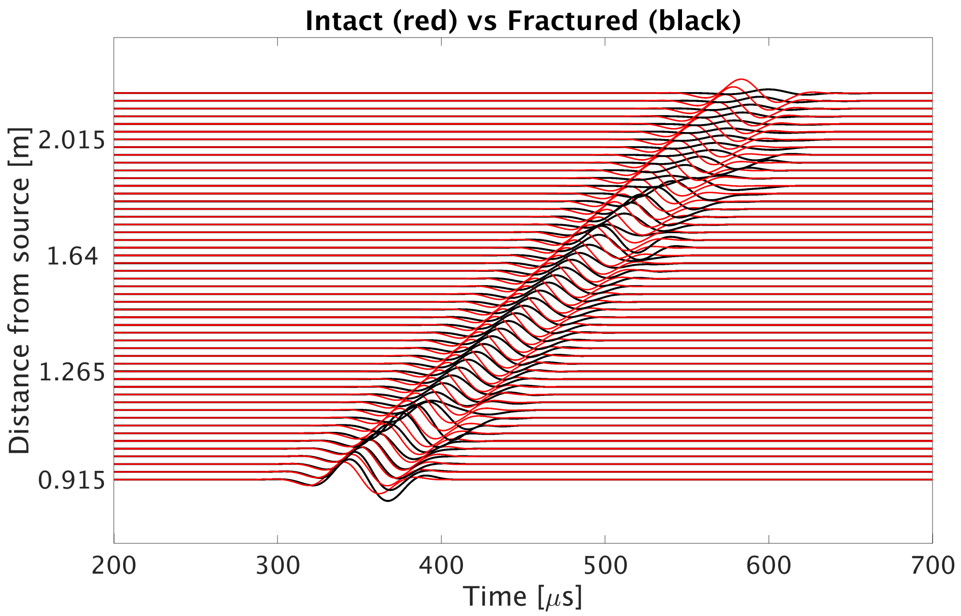

Figure 2. First-arriving P-wave extracted from the fluid pressure synthetic traces shown in Fig. 1. Red and black lines correspond to the experiments on intact and fractured rock, respectively. Depth increment between consecutive traces is 2.5 cm. The distances of the fractures from the source are 0.5 m, 1 m, and 1.75 m. Note that the amplitude and arrival time differences observed for the first traces are mainly associated with the fracture located at 0.5 m from the source, which is not visible in the considered depth range of 3 ft to 7 ft from the source.

Fig. 2 illustrates in detail the changes in the waveform of the first-arriving P-wave. We applied a time-windowing processing to isolate the first-arriving P-wave signal from the recordings shown in Fig. 1 as in Barbosa et al. (2019). In the case of an intact formation, we observe a smooth amplitude decay as the receiver distance to the source increases (red traces in Fig. 2), which is due to geometrical spreading. The black traces in Fig. 2, which correspond to a formation with fractures located at distances of 0.5 m, 1 m, and 1.75 m from the source, exhibit a more complex behavior, particularly those in close proximity to the fractures. The significant amplitude decays and time delays observed for longer offsets in the fractured case, relative to the intact rock scenario, are mainly associated with transmission losses across the fractures. We recall that by quantifying the time delays and amplitude decays, such as those observed in Fig. 2, we can estimate the associated transmission coefficient (Eq. 3) and ultimately the fracture compliance (Eq. 6).

Fig. 3 shows the transmission coefficients computed using Eq. 3 for 5 different source positions. The first source position corresponds to the case shown in Figs. 1 and 2 (Pos1 in Fig. 3), while the consecutive cases (Pos2 to Pos5) are obtained by a stepwise increase of the source depth by 30 cm. The first to fourth columns in Fig. 3 show $\ln[A^b/A^{eff}]$, δt, and the absolute value and phase of T (Eq. 3), respectively. Note that for the synthetic case, we can use very small receiver spacings and apply the method to each receiver. The receiver spacing considered in Fig. 3 is 2.5 cm, which is much smaller than the typical spacings of the order of 1 ft or $\sim$30 cm in FWS tools. The reason for this choice is to better illustrate the behavior of the numerical estimates as a function of the distance between receivers and fractures. We observe that the estimated quantities exhibit a fluctuating behavior in the proximity of the fractures, which are denoted by solid red, green, and magenta lines in Fig. 3. This is related to the extraction of the first-arriving P-wave from the recorded traces (Fig. 2). Close to the fractures, the amplitude of the first-arriving P-wave is directly affected by other scattered wavefields at the fracture (e.g., tube waves), which, in turn, has a negative impact on the estimation of the transmission coefficient. Similar effects have also been described by Barbosa et al. (2019), who demonstrated that, a larger distance between the receivers and the fracture results in more robust fracture compliance estimates. We have found that when the receiver is located at distances of at least 1/2 and 3/2 times the dominant wavelength from a deeper or a shallower fracture, respectively, the fluctuations of the estimated values decrease significantly. These noisy receiver offsets with regard to the fractures are denoted in Fig. 3 by grey areas. Following this criterion, we only use information from receivers outside the grey areas for the estimation of fracture compliance. Furthermore, in order to produce results that are comparable to a real data case, the numerical dataset used to solve Eq. 5 is composed only of the records of 5 receivers with offsets to the source ranging from 3 ft to 7 ft, whose positions are denoted by red circles in Fig. 3.

To assess the validity of the estimated transmission coefficients, we show in Fig. 3 the analytical approximation of the magnitude and phase of the transmission coefficient obtained using Eq. 4 (black dashed line). To this end, we first compute the individual fracture compliances Z_{N_i} using its common definition for very thin layers (Schoenberg, 1980), which is given by the ratio between the aperture h and the undrained P-wave modulus of the material filling the fracture. The latter is computed following Gassmann (1951). Using the Z_{N_i} values and Eq. 6, we compute the individual t_i coefficients that enter into Eq. 4 to obtain the bulk transmission coefficient of the set of fractures T. We observe that, in general, the numerical results are consistent with the analytical prediction outside the grey areas. In spite of this overall good agreement, there are some discrepancies between the analytical and numerical transmission coefficients, which can be due to: (i) errors associated with the extraction of the first arriving P-wave (Eq. 1) for the intact and fractured cases (Fig. 1); (ii) small differences in the functions F and G for intact and fractured formations (relevant for the derivation of Eq. 3); (iii) the analytical approximation of the transmission losses, which, for example, does not account for the hydraulic communication between the fractures and the borehole fluid that allows for the tube wave generation when the incident wave compresses the fracture; (iv) the limitations of Eq. 4 to reproduce the effective transmission coefficient T across multiple fractures (e.g., in the presence of fracture interaction effects); and (v) the use of the linear slip model to estimate the seismic response of relatively thick fractures at sonic frequencies (for numerical reasons, the apertures of the fractures range from 5 mm to 1 cm, which can be considered as an extreme scenario of realistic fracture apertures). We therefore consider the analytical transmission coefficient T as a guideline, rather than an exact reference, for the assessment of numerical results.

We consider the numerically estimated transmission coefficient T_j for each receiver at the 5 different source positions shown in Fig. 3 and then use Eq. 5 to find the compliance values Z_{N_i} for the three fractures present in the numerical model. As mentioned before, signals from receivers located in the grey areas of Fig. 3 are not considered in the analysis. Fig. 4 shows a comparison between the analytical approximation of the compliance of the fractures and the ones obtained with our method applied to numerical FWS data. Note that, in Fig. 4, we plot the real component of the numerically estimated compliance values whereas the analytical ones are real-valued. We refer to the latter as Z_N(HiF) as it corresponds to the high-frequency (HiF) limit of the poroelastic response of a single infinitely long fracture (Barbosa et al., 2017). Overall, the agreement is very good for the three fractures, not only with regard to the absolute values, but also in terms of the general trend of the values. This suggests that the differences in transmission coefficients observed in Fig. 3 can be considered to have a relatively small impact on the compliance estimates. The difference between numerical and analytical results is most significant for the stiffest fracture located at 1 m depth (overestimated by $\sim 40\%$) and de-

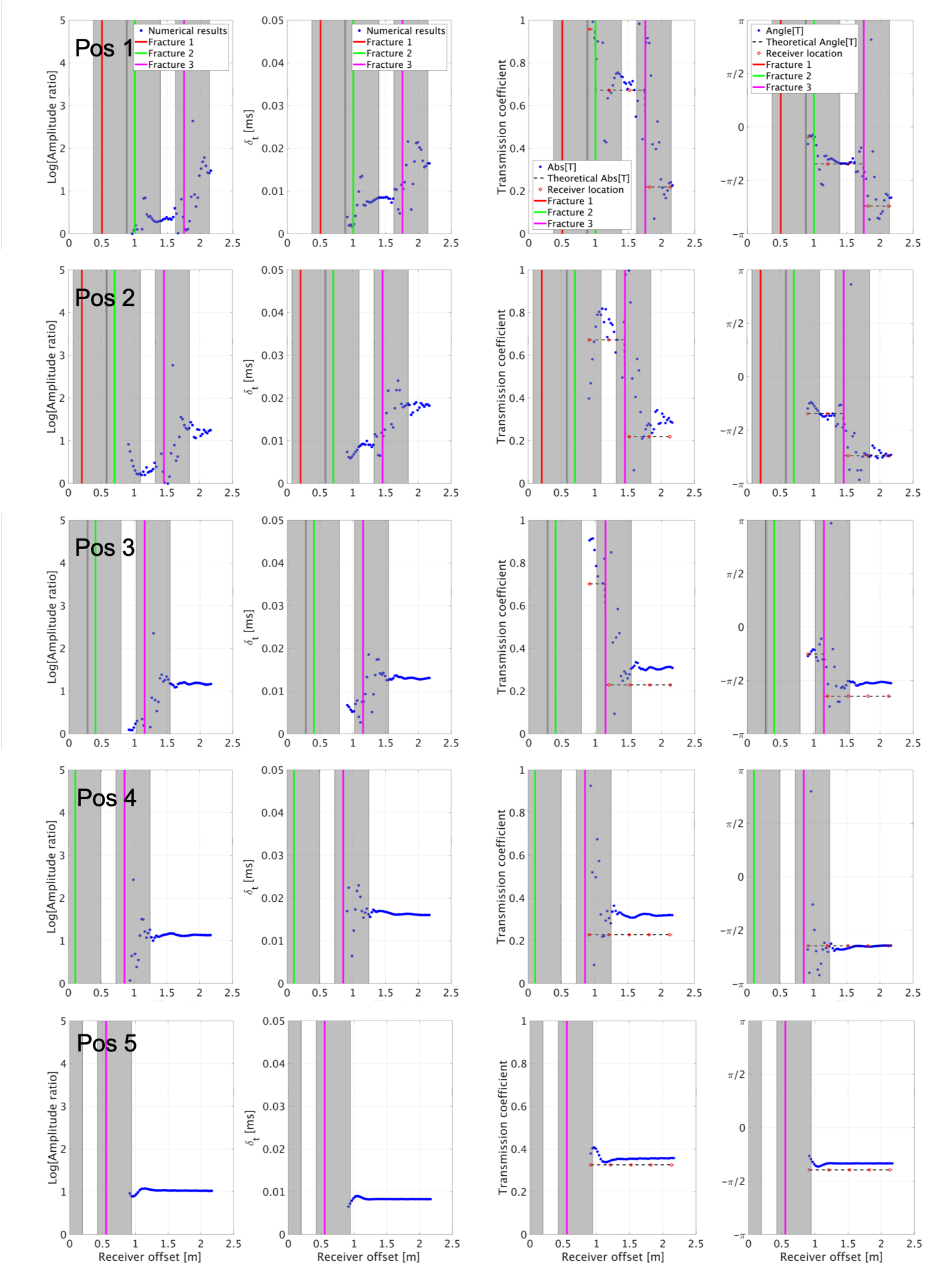

Figure 3. Numerically obtained $\ln[A^b/A^{eff}]$, δt, $|T|$, and phase of T (blue dots) for 5 source positions across a fractured formation. Fracture locations are denoted by the red, green, and magenta vertical lines, which are surrounded by grey areas characterizing by the presence of noisy traces. The magnitude and phase of the theoretical transmission coefficient (Eq. 4) is denoted by the black dashed line. Red circles illustrate the position of 5 receivers located from 3 ft to 7 ft away from the source.

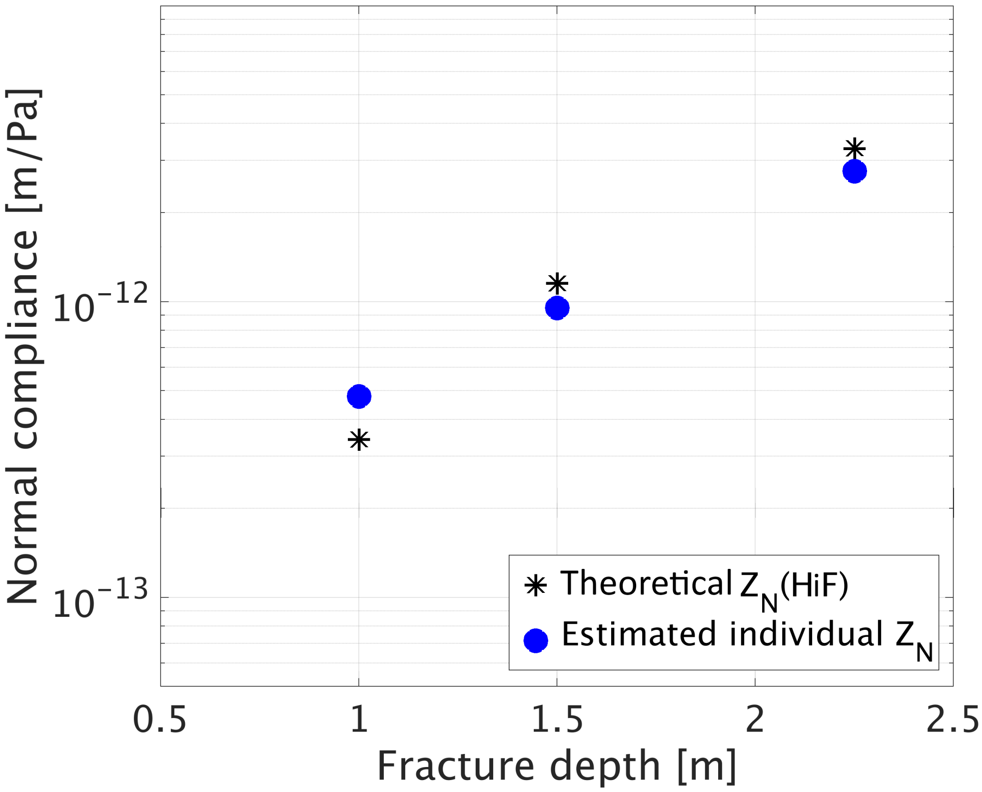

Figure 4. Numerical (dots) and analytical (stars) estimations of the normal compliance of the three fractures present in the numerical model.

creases for the more compliant fractures ($\sim 16\%$). Note that, given that the grey zones of the fractures located at 1 m and 1.5 m depth overlap, it is not possible to obtain independent information about the shallower fracture. In spite of this, the overdetermined nature of Eqs. 5, and the fact that the other two fractures can be observed independently, allows us to get reasonable compliance estimates for all the fractures. Although not shown here, we have also computed the imaginary components of the numerically inferred Z_N values. We found that the imaginary components are approximately one order-of-magnitude smaller than real components. That is, they are not negligible as predicted by the real-valued analytical solution Z_N(HiF). The reconciliation of the differences between the analytical and numerical compliance estimates follows the same reasoning as the one outlined above for the transmission coefficients (Fig. 3). In the following, we only show the real component of the estimated compliance.

Given that the FWS field data considered in this work are characterized by consecutive source positions separated by $\sim$2 ft, it is important to also show a case in which individual compliances cannot be obtained with our method. This occurs when two or more fractures cannot be observed independently in spite of the multiple source and receiver positions considered. Fig. 5 provides an example of such a scenario, in which the same three fractures described in Table 1 are located at distances of 0.45 m, 0.5 m, and 0.55 m from the source (Figs. 5a and b). If consecutive source positions always include the three fractures between the source and the receivers, then it is not possible to obtain individual transmission coefficients t_i using the estimated T_j-values. That is, Eq. 5 becomes underdetermined. As a consequence, for this subset of fractures, our method

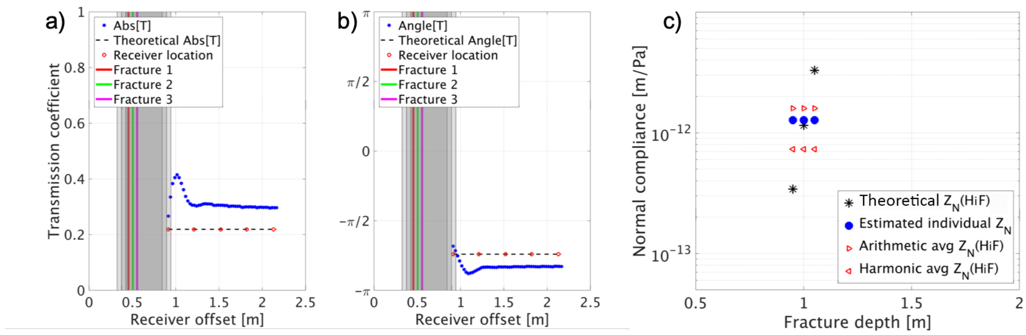

Figure 5. Numerically estimated (a) absolute value and (b) phase of the transmission coefficient T associated with the set of closely spaced fractures. Fracture locations are denoted by the red, green, and magenta vertical lines. (c) Numerically estimated (dots) and analytical (stars) compliance values for the three fractures. Triangles denote the arithmetic and harmonic averages of the analytical individual compliances.

only provides an estimate of the effective compliance. We therefore assume that all fractures in the subset are associated with the same transmission coefficient t_i to solve the system of Eqs. 5. Fig. 5c shows the result of this procedure, in which a single effective compliance value representing the overall effect of the fracture set is obtained. Note that this estimate falls between the arithmetic and harmonic averages of the individual compliance values.

3.2 Field data set

We acquired FWS logs in two boreholes at the GTS, which were drilled as part of a decameter-scale, in situ stimulation and circulation (ISC) experiment (e.g., Amann et al., 2018). The two boreholes considered here were dedicated to stimulation-type injections and are referred to as INJ1 and INJ2 (Fig. 6). They penetrate moderately fractured crystalline rocks dissected by major shear zones, which are classified as being of S1- and S3-type in Fig. 6 (Wenning et al., 2018; Krietsch et al., 2018; Brixel et al., 2020; Doetsch et al., 2020). The S3-type shear zones are associated with lamprophyre dikes. The host rock, referred to as Grimsel granodiorite, exhibits strong foliation due to aligned grains of biotite as well as bands of mylonite (Majer et al., 1990) and shows no signs of pervasive weathering. The more recent stages of brittle deformation are manifested by the presence of macroscopic fractures as well as micro-fractures.

The FWS data were acquired using a MSI 2SAA-1000-F modular multi-frequency sonic logging tool comprising a monopole source separated 91.4 cm (3 ft) from an array of five receivers spaced at 30.48 cm (1 ft) intervals. Note that this configuration is similar to the one illustrated by the red circles in Fig. 3. We considered nominal source frequencies of 15 kHz and 25 kHz. An optimal signal-to-noise ratio for the data was achieved by performing multiple static measurements, in which 15 traces were stacked at each stationary tool position. The temporal sampling rate was 4 μs.

A summary of the source positions, at which static measurements were acquired at the two boreholes, is given in Table 2. We have followed the characterization of the features intersecting the borehole (i. e., location, orientation, spacing, and width) performed by Krietsch et al. (2018) and Dutler et al. (2019) using acoustic (ATV) and optical televiewer (OTV) logs. In particular, we use this information to locate (i) the frac-

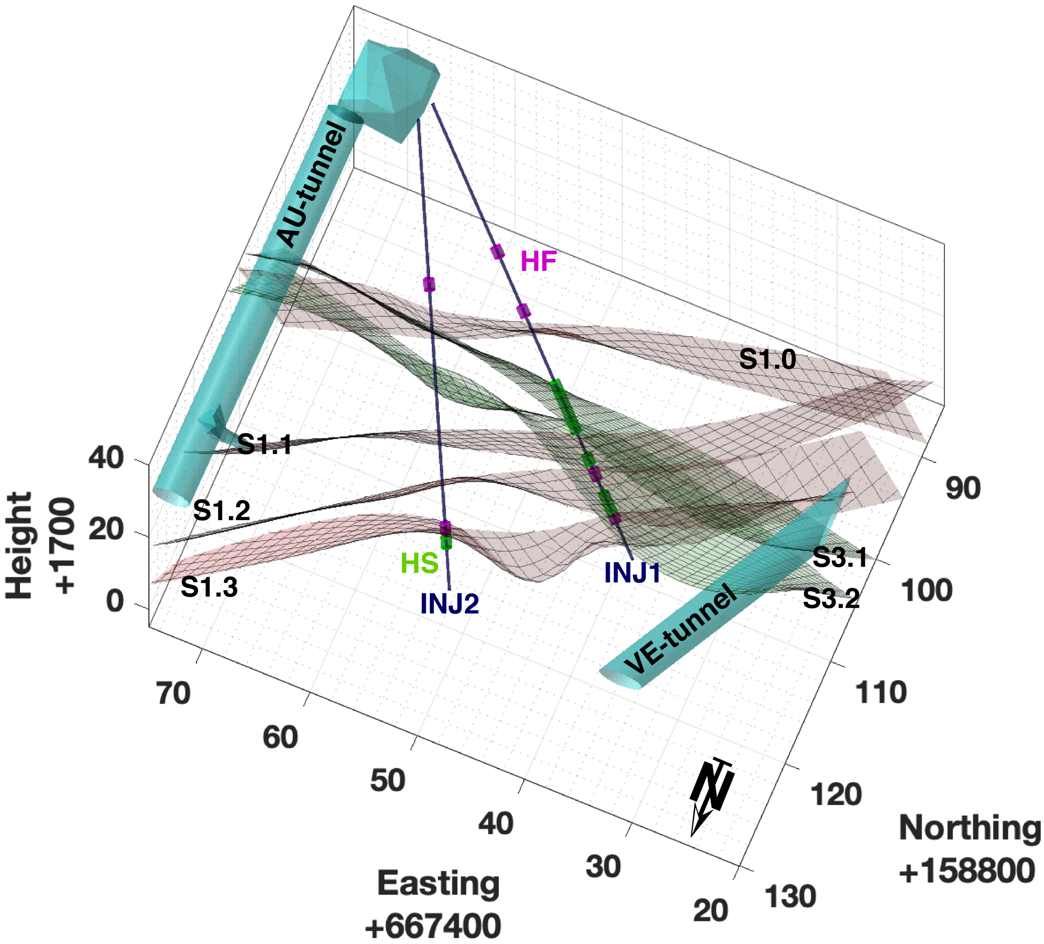

Figure 6. Locations of the considered boreholes INJ1 and INJ2 at the GTS. The two boreholes intersect six major sub-vertical ductile shear zones. Four of these shear zones follow a NE-SW strike, classified as being of S1-type, and two an E-W strike, classified as being of S3-type. Between the two S3-type shear zones the rock mass is highly fractured. The parts of the boreholes used in the hydraulic stimulation and circulation experiments performed prior to our measurements are illustrated as magenta and green intervals, respectively. HF and HS refers to hydrofracturing and hydroshearing experiments, respectively.

tures for which compliance will be estimated and (ii) the intact zones of the boreholes from where the reference signal is obtained (Brixel et al., 2020).

Figs. 7 and 8 show examples of the extracted first-arriving P wave at the 5 receivers and for 4 different source positions along INJ1 and INJ2, respectively. Red dashed curves illustrate the reference signals that are used to compute the time delays and amplitude ratios (Eq. 3). For each receiver, the reference signals are obtained by averaging the signals recorded in those positions where no fractures or other visible heterogeneities were observed in the OTV and ATV images between the source and the corresponding receiver. Note that we assign a single reference signal to the intact sections of the borehole fol-

Table 2. Source positions along boreholes INJ1 and INJ2.

	INJ1	**INJ2**
Source depth range [m]	23.77–42.67	3.04–43.28
Spatial sampling rate [m]	0.60	0.60

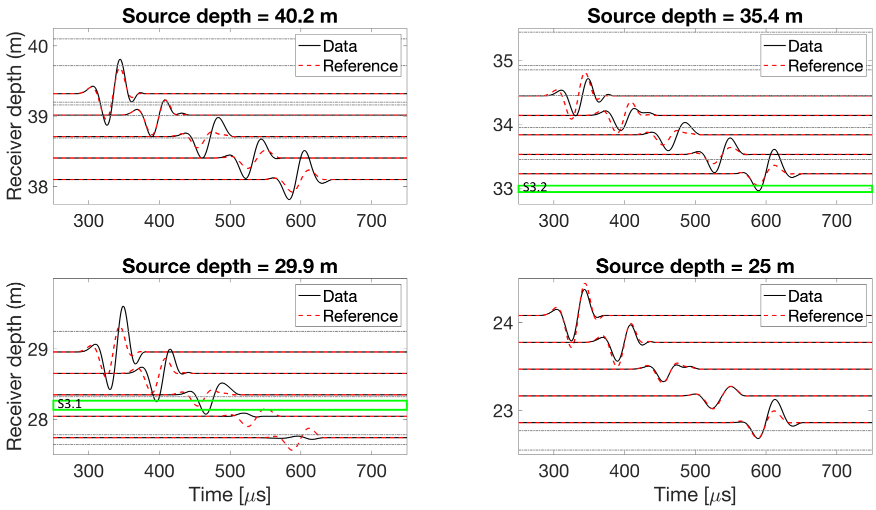

Figure 7. Examples of extracted P-wave first-arrivals at 5 receivers for 4 different source positions along the INJ1 borehole. Red dashed traces correspond to the reference signals used to compute transmission coefficients (Eq. 3). The nominal source frequency of the FWS source is 25 kHz. Grey lines and green rectangles denote fracture and S3-type shear zone locations, respectively.

lowing the results of Barbosa et al. (2019), which showed that P-wave velocities in intact sections of INJ2 exhibit little variation. When velocities measured in intact rock exhibit strong fluctuation along the borehole, the reference signal should be extracted as close as possible to the fractured section in which fracture-related time delays and amplitude decays are estimated. Moreover, our method assumes that scattering effects are exclusively related to the presence of fractures and not to abrupt changes in lithological facies along the borehole. For this reason, sections containing S3-type of shear zones have been removed from the analysis. Figs. 7 and 8 illustrate the significant impact of the S3-type shear zones on both the amplitude and arrival time of the recorded signal.

Using the extracted P-wave first-arrivals (Figs. 7 and 8), we applied the method given by Eqs. 3 to 6 to obtain the fracture compliance estimates along INJ1 and INJ2, respectively. It is important to remark that only signals recorded beyond the noisy receiver offset affected by other scattered wavefields in the vicinity of the fractures (as illustrated in Fig. 3 by grey areas) are considered for compliance estimation. In the following, we provide a discussion of the results and their implications.

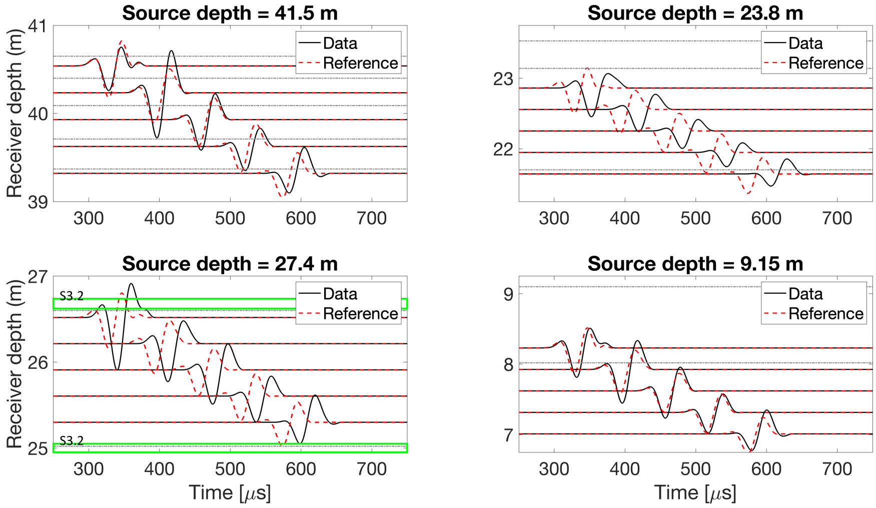

Figure 8. Examples of extracted P-wave first-arrivals at 5 receivers for 4 different source positions along the INJ2 borehole. Red dashed traces correspond to the reference signals used to compute transmission coefficients (Eq. 3). The nominal source frequency of the FWS source is 25 kHz. Grey lines and green rectangles denote fracture and S3-type shear zone locations, respectively.

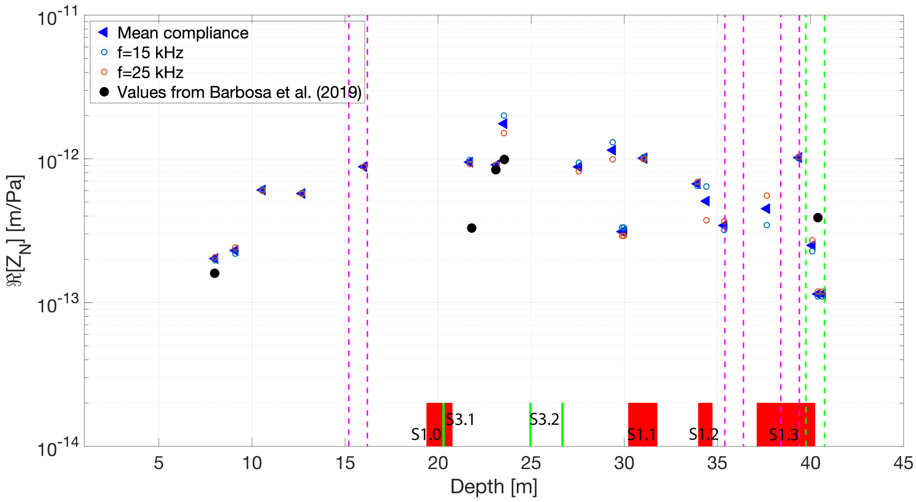

Figure 9. Real component of the compliance of fractures intersecting the INJ2 borehole. Blue triangles and black circles denote the compliance estimates from this work and from Barbosa et al. (2019), respectively, which both correspond to the arithmetic mean of values obtained for 15 kHz (blue circle) and 25 kHz (red circle). Red and green markers denote S1- and S3-type shear zones, respectively. Magenta and green dashed lines denote borehole intervals where hydrofracturing and hydroshearing experiments, respectively, were carried out after the measurements of Barbosa et al. (2019)

3.2.1 Relation with previous estimates

Let us first consider Fig. 9, which presents results for INJ2 (blue triangles). For comparison, we plot the results obtained by Barbosa et al. (2019) for 5 isolated fractures intersecting the same borehole (black circles), which, in the following, are referred to as the old estimates. Both sets of compliance estimates correspond to the arithmetic mean of the values obtained for nominal source center frequencies of 15 kHz and 25 kHz, which are denoted by blue and red circles in Fig. 9, respectively. Overall, the agreement between the old and new estimates is good in terms of magnitude and depth variation. We observe a general increase in fracture compliance towards the S3-type shear zones, as denoted by green markers in Fig. 9, located at ∼20 m to ∼27 m borehole depth. As mentioned before, an advantage of the new method over the one presented in Barbosa et al. (2019) is that fractures do not need to be isolated, which allows us to obtain a profile of fracture compliance along the borehole depth.

In spite of the overall consistency, discrepancies in the magnitude of old and new compliance estimates are noticeable for some fractures (e.g., fractures at 21.8 m and 40.4 m depth). The methodological aspects that contribute to the observed differences include the following:

- With the old method, the estimated attenuation has to be corrected for intrinsic background attenuation and geometrical spreading in order to obtain the transmission coefficient associated with a given fracture. The latter implies assuming or determining the function describing the amplitude decay of head waves travelling along a borehole (Barbosa et al., 2019). With the new method, these corrections are assumed to be the same for intact and fractured sections, thus, simplifying the procedure to obtain the transmission coefficient.

- The old method relies on comparing the signals recorded at two receivers. Barbosa et al. (2019) used a tool containing 3 receivers spaced at 1 ft intervals, but only the estimates related to the first and last receivers, spaced at 2 ft, were considered to estimate compliance. With the new method, a reference signal, representing the propagation across intact background rock, is compared with the signals recorded at intervals containing fractures. In the new data set, the tool consisted of 5 receivers. As a consequence, for each source position, up to five signals were used to constrain fracture compliance as opposed to only one with the old method.

- The new method combines information about the transmission coefficient associated with different fractures or sets of fractures to provide individual fracture compliance estimates. Correspondingly, the overall solution of the system of Eqs. 5 is determined through a least squares procedure. With the old method, one collects information on the individual fractures only, which, in turn, is expected to increase its accuracy as compared with a least squares solution for a set of fractures. Indeed, although not shown for brevity, using numerical simulations, we found that when the new method is applied in a single fracture scenario, compliance estimates are slightly closer to the analytical values than for sets of fractures. It is important to mention, however, that part of this behavior could be associated to the correctness of the analytical approximation of the fracture compliance (as discussed in Section 3.1).

Finally, it is worth mentioning that the time elapsed between the old and new measurements is approximately 2 years. During this period, several hydraulic shearing (HS) and hydraulic fracturing (HF) experiments were carried out in INJ1 and INJ2 as part of the ISC project (Dutler et al., 2019; Krietsch et al., 2020). The location of these experiments is denoted by the magenta (HF) and green (HS) dashed lines in Fig. 9. For this reason, although the FWS signals used in both methods are similar, the environment through which they propagate may have undergone some changes. These changes could be particularly relevant for the data acquired around ∼40 m depth. This region was affected by HS experiments (Krietsch et al., 2020) as well as by steeply inclined hydrofractures created by the later experiments of Dutler et al. (2019) and where our results exhibit the largest discrepancies between the old and new estimates.

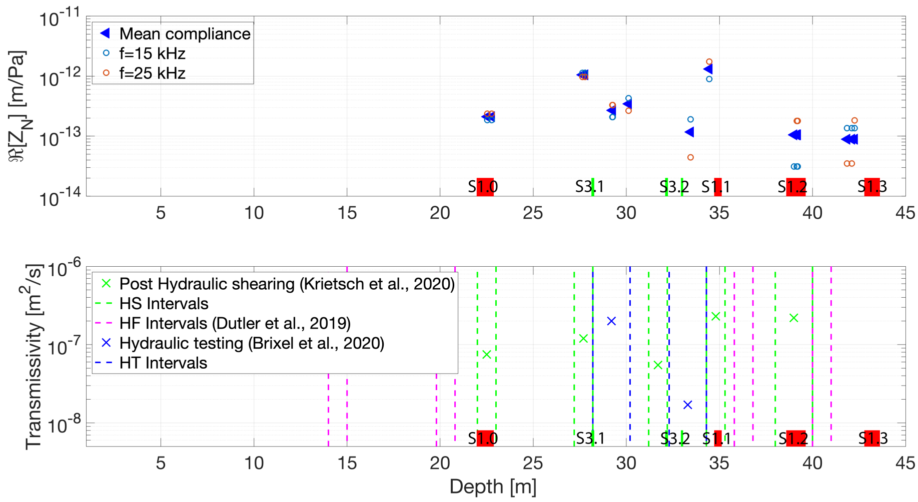

Figure 10. a) Real component of the compliance of fractures intersecting the INJ1 borehole (blue triangles). Values correspond to the arithmetic mean of values obtained for 15 kHz (blue circle) and 25 kHz (red circle). Red and green markers denote the depths of S1 and S3 shear zones, respectively. b) Green and blue crosses denote transmissivity values obtained by Krietsch et al. (2020) and Brixel et al. (2020), respectively. Blue, magenta, and green dashed lines denote borehole intervals used in the experiments of Brixel et al. (2020), Dutler et al. (2019), and Krietsch et al. (2020), respectively.

3.2.2 Relation between hydraulic and mechanical fracture behavior

Fig. 10a shows the compliance estimates for the INJ1 borehole. The depth range of the data set is shorter than for INJ2 (Table 2) and mainly covers the S1-type (red dots) and S3-type (green dots) shear zones. It is important to mention that, for this borehole, there are no previous compliance estimates. However, transmissivity estimates from hydraulic tests have been reported (Krietsch et al., 2020; Brixel et al., 2020), which, in the context of this work, are useful to qualitatively analyze the hydromechanical coupling of the fractures. The hydraulic tests performed by Brixel et al. (2020) determined the transmissivity of both the non-fractured and fractured sections to explore the hydraulic behavior of the shear zones as a function of fracture density. The transmissivity values obtained for intervals containing fractures range from 10^{-12} m^2/s to 10^{-6} m^2/s. Here, we consider only transmissivity values obtained for short testing intervals of 1 to 2 m length, referred to as high-resolution tests, for which the length of the support volume sampled by the hydraulic test remained shorter than 5 m, as inferred from the lack of response detected in adjacent observation boreholes. Like this, both transmissivity and compliance values are mainly representative of the immediate vicinity of the borehole. In addition, we do not show values obtained from intervals that could have been affected by the HF or HS experiments of Krietsch et al. (2020) and Dutler et al. (2019), which were performed after the measurements of Brixel et al. (2020).

Overall, we observe that the fracture compliance estimates tend to follow the transmissivity profile (Fig. 10), that is, higher transmissivities are, in general, associated with more compliant fractures. Interestingly, fracture compliance estimates from FWS data are generally associated with the unrelaxed or high-frequency limit, in which there is no hydraulic communication between the fracture and the embedding background. Thus, normal-to-the-fracture permeability has limited impact on the estimated compliance. Moreover, it has been shown that the scattering of seismic waves from fractures is also not directly influenced by the permeability along the fracture in the case of transversely isotropic fractures (e.g., Nakagawa & Schoenberg, 2007). Lastly, the good agreement between the estimated compliance values and the analytical solution for planar thin-layers shown in Section 3.1 imply that the impact of tube wave energy conversion at the fracture, which can be related to the permeability of fractures (e.g., Bakku et al., 2013), on the estimated compliance is small. Thus, while transmission losses across fractures are highly dependent on fracture compliance, this theoretical evidence points to a lack of sensitivity with regard to fracture permeability. Nevertheless, as pointed out by several authors (e.g., Zimmerman & Main, 2004; Pyrak-Nolte & Nolte, 2016), the internal structure of fractures controls both their capacity to let fluid to flow and their deformation upon loading. This, in turn, is expected to manifest itself as an interdependence between the mechanical and hydraulic behavior of fractures. The observed correlation between the hydraulic response and the compliance of fractures in Fig. 10 provide further evidence to such hydromechanical coupling of fractures and suggests that compliance profiles inferred from FWS data could be used for identifying the most permeable sections along a borehole.

A closer inspection of the results shown in Fig. 10 indicates that the fractures in the interval between 38 m and 40 m depth seem to be less compliant than expected. This could be related to the large number of fractures present in the interval. Indeed, this interval contains 5 fractures according to the OTV and ATV images. However, after applying the criterion for the minimum receiver offset to the fractures, and due to the proximity between some of the fractures, we could only get an effective compliance estimate for a subset of three fractures from the data and the other two fractures could not be characterized at all (Fig. 10a). Furthermore, Dutler et al. (2019) performed HF experiments (denoted by the magenta dashed lines in Fig. 10b), which resulted in long hydrofractures quasi-parallel to the borehole axis that intersect most of the fractures of this interval. Thus, the unexpected hydromechanical relation could also be associated with the effects of the hydraulic connectivity between the pre-existing fractures and the newly-created hydrofractures.

It is important to mention that, even though we only show two values from the work of Brixel et al. (2020), they also found the highest transmissivity values next to S3.1 and S3.2 shear zones, for which volumetric fracture density is the largest. Furthermore, Brixel et al. (2020) observed either no correlation or a weakly negative correlation between transmissivity and fracture density in the interval between the S1.1 and S1.2 fracture zones, which was attributed to asymmetrical variations in fracture density next to discrete faults. Interestingly, this interval of weak correlation also exhibits an unexpected hydromechanical correlation as the one we described above (Fig. 10).

Brixel et al. (2020) also provide transmissivity estimates from high-resolution hydraulic tests in INJ2. However, only three of the corresponding borehole intervals were not potentially affected by the tests performed by Dutler et al. (2019); Krietsch et al. (2020). Two of these intervals correspond to intervals for which we did not obtained compliance values. For this reason, we do not show a hydromechanical comparison for INJ2. Nevertheless, Brixel et al. (2020) mentioned that no pressure pulse could be induced for the fracture located at a distance of $\sim$1.5 m from the S3.2 fracture zone (Fig. 9). This is an indication of the presence of a highly permeable fracture, for which they could only assign a lower-bound transmissivity value of 10^{-5} m^2/s based on the upper limit of the test apparatus. Fig. 9 shows that this highly transmissive fracture is associated with the highest fracture compliance observed along INJ2.

3.2.3 Relation between INJ1 and INJ2 estimates

Finally, by comparing Figs. 9 and 10a, we observe that the two sets of compliance estimates are consistent with each other. Compliance values across the S1- and S3-type shear zones mainly oscillate between 1e-13 m/Pa and 1e-12 m/Pa. More importantly, the overall variation of the compliance across the shear zones is similar, with increasing values towards the S3.1 shear zone in both boreholes. Similarly, compliance estimates tend to increase close to the S1.1 shear zone, which intersects INJ1 and INJ2 at ∼35 m and ∼31 m depth, respectively.

From the analysis of transmissivity estimates across the different shear zones intersecting INJ1 and INJ2, Brixel et al. (2020) pointed out that fracture permeability tends to increase from the host rock to the core of the shear zones. This behaviour was attributed to possible differences in aperture, length, orientation, and degree of interconnectivity of fractures in different regions of the borehole. Overall, our compliance estimates reproduce the same trend for both boreholes, showing lower compliance estimates towards the intact host rock.

Wenning et al. (2018) describe the S3-type shear zones as "mature" brittle faults with a pronounced damage zone (DZ) and altered fault core composition. As a consequence, lower velocities (associated with the presence of compliant fractures in the DZ) and higher transmissivities were predicted by Wenning et al. (2018) in the vicinity of S3-type shear zones. Our compliance estimates are consistent with this conceptual model in both boreholes. Doetsch et al. (2020) provided a seismic characterization of the same rock volume prior to hydraulic stimulations and found that the S3-type shear zones are characterized by reduced seismic wave velocities with respect to the host rock. They argue that a higher fracture density could be the controlling factor associated with the velocity decrease. Our results show that decreasing velocities could not only be associated with variations in fracture density but also in fracture compliance, which was found to vary by an order-of-magnitude along a ∼30 m borehole section. This further suggests that compliance estimates from FWS data can provide valuable insight prior to hydraulic stimulation experiments. Doetsch et al. (2020) also pointed out that the elevated fracture density at ∼43 m depth in INJ1 does not manifest itself with a clear decrease in seismic velocity. Here, the lack of correlation between high fracture density and low velocity zones in the 3D seismic volume obtained by Doetsch et al. (2020), could be explained by the low compliance exhibited by the fractures close to the S1.3 shear zone.

Finally, it is important to remark that Eq. 6 is strictly valid only when considering the transmission coefficient at normal P-wave incidence. Barbosa et al. (2019) has shown that when fractures are not normal to the borehole axis, an underestimation of the transmission coefficient and, consequently, an overestimation of the fracture compliance is expected. Corresponding errors are expected to be negligible except for high angle fractures (greater than 60°) acutely intersecting the borehole. OTV and ATV images reported in previous works for INJ1 and INJ2 boreholes (e.g., Dutler et al., 2019; Barbosa et al., 2019; Krietsch et al., 2020) showed that most fractures are not perpendicular to the axis of the borehole. Furthermore, the orientations of INJ1 and INJ2 render the intersection angles between the fractures and the borehole axes different for both boreholes. In spite of this, estimates from the two boreholes are remarkably consistent, which, in turn, implies that the corresponding errors are not contributing significantly to the observed compliance variation along the boreholes.

4 Discussion

Unlike the method of Barbosa et al. (2019) for single fractures, the newly proposed approach allows for characterizing a set of fractures located in the interval between the source and the receivers of the sonic tool. This makes it particularly useful when dealing with conventional non-static FWS data from heavily fractured borehole sections. In the context of FWS experiments, wavelengths are expected to be smaller than the length of the fractures but can be comparable or larger than the distance between adjacent fractures. Thus, the proposed methodology can be considered as a hybrid between effective medium (e.g., Prioul et al., 2007; Prioul & Jocker, 2009) and discrete approches (e.g., Barbosa et al., 2019). In some cases, the separation between fractures allows for a discrete treatment, in which individual fracture compliances are estimated, whereas in other situations, the fractures are so close together that their joint effects can only be treated in an effective way.This relates to the system of equations solved to find the transmission coefficients associated with each fracture (Eqs. 5). When the system of equations relating the observed transmission coefficient with the individual coefficients of each fracture becomes overdetermined, we can obtain an independent compliance value for each fracture intersecting the borehole. In some cases, the system of equations becomes underdetermined because a subset of two or more fractures are always observed together. In this case, fractures are assumed to have the same compliance and an effective compliance for the subset is obtained. Using numerical modelling, we have shown that this effective compliance lies between the arithmetic and harmonic averages of their true compliances.

When comparing the two cases analyzed in Section 3.1, we observe that the differences between the analytical and numerical estimates of the transmission coefficients are similar, regardless of the distance between fractures. One important point of reducing the distance between fractures is that, in general, the compliance of one fracture, and the corresponding effects on wave propagation, can be affected by the elastic interaction with adjacent fractures, which, in turn, could impact on the estimated transmission losses. In this sense, Cai and Zhao (2000) studied wave propagation across multiple parallel fractures and analyzed the effects of interactions between multiple wave reflections and transmissions on the Eq. 4. They argue that Eq. 4 may not be applicable if the effects of multiple reflections are significant due to the close spacing of the fractures. The limit of validity proposed by the authors is given by the ratio between the fracture spacing and the prevailing wavelength. When this ratio is much lower than 1, the effective transmission coefficient depends on the distance between fractures and Eq. 4 is not strictly valid anymore. For the smallest spacing considered in this work, the ratio is ~ 0.2, for which we still obtain expected values for the real component of Z_N (Fig. 5). This means that any prevailing fracture interaction effects do not affect significantly the real component of our compliance estimates.

It is important to note that the proposed methodology provides frequency-dependent and complex-valued fracture compliances. Complex-valued fracture compliance can occur in fluid-saturated environments, for example, when the so-called wave-induced fluid flow (WIFF) between the fracture and the embedding background produces sufficient seismic energy dissipation. For a low-permeability background and at sonic frequencies, however, WIFF effects are expected to be negligible. Although the imaginary part may still be non-negligible, we have not analyzed this component in detail as there are no analytical solutions for the frequency-dependent compliance of a fracture intersecting a borehole. A first-order approximation corresponds to the thin-layer model considered in this work. In this case, the imaginary component is expected to be negligible for the petrophysical properties considered. Conversely, our results showed that the imaginary component is one order-of-magnitude smaller than the real component but it is not negligible even in a single-fracture scenario. This implies that the imaginary component of the compliance can be more affected by the assumptions of our method, as described in the analysis of Fig. 3. In this context, it is interesting to note that, the impact of elastic stress interaction due to the presence of multiple fractures on the imaginary component of the compliance remains unexplored.

5 Conclusions

We have presented a new methodology for the quasi-continuous estimation of fracture compliance along a borehole based on the time delays and amplitude decays experienced by the critically refracted P-wave. By quantifying them, we can compute the transmission coefficient associated with a given individual fracture, which is then used to estimate fracture compliance. We have validated the method using numerical simulations, for which the estimated fracture compliances were found to be in good agreement with corresponding analytical approximations.

We then applied the method to FWS data acquired along two boreholes penetrating moderately fractured granodioritic rock. The required reference values were estimated from the sections of the borehole that did not exhibit any visible fractures or other mechanical damage in OTV and ATV images. Our estimates of mechanical normal compliance are consistent with previously reported values for the same site. Interestingly, even though the estimated compliance values are representative of the vicinity of the borehole, compliance profiles from two boreholes intersecting the same shear zones exhibit comparable values. Finally, comparison between the compliance profiles obtained from FWS log data and transmissivity values from hydraulic experiments suggests that the former can be a valuable tool for identifying the most permeable fractures of a borehole.

Acknowledgments

This work was supported by grants from the Swiss National Science Foundation (Grant numbers 166900, 178946, and 196037) and completed within SCCER-SOE with the support of Innosuisse. We thank Joseph Doetsch for offering support and access to the GTS for the field experiments. Jürg Hunziker provided helpful advice on the numerical modeling. We appreciate the comments from two anonymous reviewers and the associate editor that helped to improve the quality of this manuscript. The data for this paper are available at `http://doi.org/10.5281/zenodo.4072839`.

References

Amann, F., Gischig, V., Evans, K., Doetsch, J., Jalali, R., Valley, B., ... Giardini, D. (2018). The seismo-hydromechanical behavior during deep geothermal reservoir stimulations: open questions tackled in a decameter-scale in situ stimulation experiment. *Solid Earth*, *9*(1), 115–137.

Bakku, S. K., Fehler, M., & Burns, D. (2013). Fracture compliance estimation using borehole tube waves. *Geophysics*, *78*(4), D249–D260.

Barbosa, N. D., Caspari, E., Greenwood, A., & Holliger, K. (2020). Estimation of the effective compliance of a set of fractures using full-waveform sonic log data. In *Seg technical program expanded abstracts 2020* (pp. 460–464). Society of Exploration Geophysicists.

Barbosa, N. D., Caspari, E., Rubino, J. G., Greenwood, A., Baron, L., & Holliger, K. (2019). Estimation of fracture compliance from attenuation and velocity analysis of full-waveform sonic log data. *Journal of Geophysical Research: Solid Earth*, *124*(3), 2738–2761.

Barbosa, N. D., Köpke, C., Caspari, E., Germán Rubino, J., Irving, J., & Holliger, K. (2020). Impact of poroelastic effects on the inversion of fracture properties from AVOAz data in HTI media. *Geophysics*, *85*(5), 1–48.

Barbosa, N. D., Rubino, J. G., Caspari, E., & Holliger, K. (2017). Extension of the classical linear slip model for fluid-saturated fractures: Accounting for fluid pressure diffusion effects. *Journal of Geophysical Research: Solid Earth*, *122*(2), 1302–1323.

Biot, M. A. (1962). Mechanics of deformation and acoustic propagation in porous media. *Journal of Applied Physics*, *33*, 1482-1498.

Brixel, B., Klepikova, M., Jalali, M. R., Lei, Q., Roques, C., Kriestch, H., & Loew, S. (2020). Tracking fluid flow in shallow crustal fault zones: 1. insights from single-hole permeability estimates. *Journal of Geophysical Research: Solid Earth*, *125*(4), e2019JB018200.

Cai, J., & Zhao, J. (2000). Effects of multiple parallel fractures on apparent attenuation of stress waves in rock masses. *International Journal of Rock Mechanics and Mining Sciences*, *37*(4), 661–682.
Chapman, M. (2003). Frequency-dependent anisotropy due to meso-scale fractures in the presence of equant porosity. *Geophysical Prospecting*, *51*(5), 369–379.
Cheng, C. H., Toksöz, M. N., & Willis, M. E. (1982). Determination of in situ attenuation from full waveform acoustic logs. *Journal of Geophysical Research: Solid Earth*, *87*(B7), 5477–5484.
Cheng, Y., & Renner, J. (2018). Exploratory use of periodic pumping tests for hydraulic characterization of faults. *Geophysical Journal International*, *212*(1), 543–565.
Doetsch, J., Krietsch, H., Schmelzbach, C., Jalali, M., Gischig, V. S., Villiger, L., ... Maurer, H. (2020). Characterizing a decametre-scale granitic reservoir using GPR and seismic methods–a case study for preparing hydraulic stimulations. *Solid Earth Discussions*, 1–28.
Durán, E. L., van Wijk, K., Adam, L., & Wallis, I. C. (2018). Separating intrinsic and scattering attenuation in full waveform sonic logging with radiative transfer theory. *Geophysical Journal International*, *213*(2), 757–769.
Dutler, N., Valley, B., Gischig, V., Villiger, L., Krietsch, H., Doetsch, J., ... Amann, F. (2019). Hydraulic fracture propagation in a heterogeneous stress field in a crystalline rock mass. *Solid Earth*, *10*(6), 1877–1904.
Fang, X., Zheng, Y., & Fehler, M. C. (2016). Fracture clustering effect on amplitude variation with offset and azimuth analyses. *Geophysics*, *82*(1), N13–N25.
Gassmann, F. (1951). Elasticity of porous media. *Vierteljahrsschrder Naturforschenden Gesselschaft*, *96*(1–23).
Gudmundsson, A. (2011). *Rock fractures in geological processes.* Cambridge University Press.
Gurevich, B. (2003). Elastic properties of saturated porous rocks with aligned fractures. *Journal of Applied Geophysics*, *54*(3), 203–218.
Haldorsen, J. B., Johnson, D. L., Plona, T., Sinha, B., Valero, H.-P., & Winkler, K. (2006). Borehole acoustic waves. *Oilfield Review*, *18*(1), 34–43.
Hudson, J. A. (1980). Overall properties of a cracked solid. In *Mathematical proceedings of the cambridge philosophical society* (Vol. 88, pp. 371–384).
Hunziker, J., Greenwood, A., Minato, S., Barbosa, N. D., Caspari, E., & Holliger, K. (2020). Bayesian full-waveform inversion of tube waves to estimate fracture aperture and compliance. *Solid Earth*, *11*(2).
Kang, P. K., Zheng, Y., Fang, X., Wojcik, R., McLaughlin, D., Brown, S., ... Juanes, R. (2016). Sequential approach to joint flow-seismic inversion for improved characterization of fractured media. *Water Resources Research*, *52*(2), 903–919.
Krietsch, H., Doetsch, J., Dutler, N., Jalali, M., Gischig, V., Loew, S., & Amann, F. (2018). Comprehensive geological dataset for a fractured crystalline rock volume at the grimsel test site.
Krietsch, H., Gischig, V. S., Doetsch, J., Evans, K. F., Villiger, L., Jalali, M., ... Amann, F. (2020). Hydromechanical processes and their influence on the stimulation effected volume: observations from a decameter-scale hydraulic stimulation project. *Solid Earth*, *11*(5), 1699–1729.
Liu, E., & Martinez, A. (2013). *Seismic fracture characterization: Concepts and practical applications.* EAGE.
Lubbe, R., & Worthington, M. (2006). A field investigation of fracture compliance. *Geophysical Prospecting*, *54*(3), 319–331.
Majer, E. L., Myer, L., Peterson, J., Karasaki, K., Long, J., Martel, S., ... Vomvoris, S. (1990). *Joint seismic, hydrogeological, and geomechanical investigations of a fracture zone in the Grimsel Rock Laboratory, Switzerland* (Tech. Rep.). Lawrence Berkeley Lab., CA (USA); Nationale Genossenschaft

fuer die Lagerung Radioaktiver Abfaelle (NAGRA), Baden (Switzerland).
Milani, M., Rubino, J. G., Baron, L., Sidler, R., & Holliger, K. (2015). Attenuation of sonic waves in water-saturated alluvial sediments due to wave-induced fluid flow at microscopic, mesoscopic and macroscopic scales. *Geophysical Journal International*, *203*(1), 146–157.
Minato, S., & Ghose, R. (2016). AVO inversion for a non-welded interface: estimating compliances of a fluid-filled fracture. *Geophysical Journal International*, *206*(1), 56–62.
Molyneux, J. B., & Schmitt, D. R. (2000). Compressional-wave velocities in attenuating media: A laboratory physical model study. *Geophysics*, *65*(4), 1162–1167.
Morris, R. L., Grine, D. R., & Arkfeld, T. E. (1964). Using compressional and shear acoustic amplitudes for the location of fractures. *Journal of Petroleum Technology*, *16*(06), 623–632.
Nakagawa, S., & Schoenberg, M. A. (2007). Poroelastic modeling of seismic boundary conditions across a fracture. *The Journal of the Acoustical Society of America*, *122*(2), 831–847.
National Research Council. (1996). *Rock fractures and fluid flow: contemporary understanding and applications*. National Academies Press.
Prioul, R., Donald, A., Koepsell, R., Marzouki, Z. E., & Bratton, T. (2007). Forward modeling of fracture-induced sonic anisotropy using a combination of borehole image and sonic logs. *Geophysics*, *72*(4), E135–E147.
Prioul, R., & Jocker, J. (2009). Fracture characterization at multiple scales using borehole images, sonic logs, and walkaround vertical seismic profile. *AAPG bulletin*, *93*(11), 1503–1516.
Pyrak-Nolte, L. J., & Morris, J. (2000). Single fractures under normal stress: The relation between fracture specific stiffness and fluid flow. *International Journal of Rock Mechanics and Mining Sciences*, *37*(1-2), 245–262.
Pyrak-Nolte, L. J., Myer, L. R., & Cook, N. G. (1990a). Anisotropy in seismic velocities and amplitudes from multiple parallel fractures. *Journal of Geophysical Research: Solid Earth*, *95*(B7), 11345–11358.
Pyrak-Nolte, L. J., Myer, L. R., & Cook, N. G. (1990b). Transmission of seismic waves across single natural fractures. *Journal of Geophysical Research: Solid Earth*, *95*(B6), 8617–8638.
Pyrak-Nolte, L. J., & Nolte, D. D. (2016). Approaching a universal scaling relationship between fracture stiffness and fluid flow. *Nature communications*, *7*, 10663.
Rubino, J. G., Guarracino, L., Müller, T. M., & Holliger, K. (2013). Do seismic waves sense fracture connectivity?. *Geophysical Research Letters*, *40*(4), 692–696.
Schoenberg, M. (1980). Elastic wave behavior across linear slip interfaces. *The Journal of the Acoustical Society of America*, *68*(5), 1516–1521.
Schoenberg, M., & Douma, J. (1988). Elastic wave propagation in media with parallel fractures and aligned cracks. *Geophysical Prospecting*, *36*(6), 571–590.
Shakas, A., Maurer, H., Giertzuch, P.-L., Hertrich, M., Giardini, D., Serbetto, F., & Meier, P. (2020). Permeability enhancement from a hydraulic stimulation imaged with ground penetrating radar. *Geophysical Research Letters*, e2020GL088783.
Sidler, R., Carcione, J. M., & Holliger, K. (2013a). A pseudospectral method for the simulation of 3-D ultrasonic and seismic waves in heterogeneous poroelastic borehole environments. *Geophysical Journal International*, *196*(2), 1134–1151.
Sidler, R., Carcione, J. M., & Holliger, K. (2013b). A pseudo-spectral method for the simulation of poro-elastic seismic wave propagation in 2D polar coordinates using domain decomposition. *Journal of Computational Physics*, *235*, 846–864.

Sun, X., Tang, X., Cheng, C., & Frazer, L. N. (2000). P- and S-wave attenuation logs from monopole sonic data. *Geophysics*, *65*(3), 755–765.
Toksoz, M. N., Cheng, C. H., & Willis, M. E. (1983). *Seismic waves in a borehole - a review* (Tech. Rep.). Massachusetts Institute of Technology. Earth Resources Laboratory.
Wenning, Q. C., Madonna, C., de Haller, A., & Burg, J.-P. (2018). Permeability and seismic velocity anisotropy across a ductile-brittle fault zone in crystalline rock. *Solid Earth*, *9*, 683–698.
Worthington, M., & Hudson, J. (2000). Fault properties from seismic Q. *Geophysical Journal International*, *143*(3), 937–944.
Zimmerman, R., & Main, I. (2004). Hydromechanical behavior of fractured rocks. *International Geophysics Series*, *89*, 363–422.